Mixing in Active Turbulence: from fully developed turbulence to labyrinthine arrest

Author: Eduardo Dejuán Bitriá*
Master en Física dels Sistemes Complexos i Biofísica.
Facultat de Física, Universitat de Barcelona, Martí i Franquès 1, 08028 Barcelona, Spain.†

Advisor: Jaume Casademunt
Departament de Física de la Matèria Condensada, Universitat de Barcelona,
Institute of Complex Systems (UBICS), Barcelona, Spain; email: jaume.casademunt@ub.edu
(Dated: June 30, 2025)

Abstract: Active fluids represent a new paradigm in non-equilibrium physics. Even at low Reynolds numbers, they can develop spontaneous flows that resemble inertial turbulence in their chaotic behaviour, also with a universal scaling law. However, unlike classical turbulence, active turbulence lacks an energy cascade. Instead, it self-organizes the scales at which energy is injected and dissipated. This suggests we may be dealing with a new class of turbulence—one we are still learning how to describe. This thesis is the first to study mixing in this rich scenario, in which two qualitatively different turbulence limits emerge: one characterized by fully developed turbulence and another where labyrinth-like patterns form and the system becomes dynamically arrested. We study the mixing of a passive scalar and the movement of tracer particles within these simulated flows. We aim to characterize each flow regime using our mixing analysis. We find that tracer particles provide a more effective way to probe the transport properties of each regime, particularly through quantities like the ballistic time and the excess kurtosis, which clearly distinguish the two types of flow and point towards a non-diffusive stationary state of the labyrinths. Interestingly, also in the labyrinthine regime, tracer particles show a heavy-tailed distribution in concentration, indicating clustering and the possible formation of particle caustics. Although this study is still in progress, our results already point toward labyrinthine flows as a distinct form of quantitative and qualitative turbulence, with unique transport properties.

I. INTRODUCTION

Turbulence is found everywhere. From cooking to interstellar gas clouds. And though it is regarded as the last unsolved problem in classical physics, its study has benefited many neighbouring areas of physics. Concepts such as scale-invariance, universality, and anomalous diffusion—now fundamental in many fields—were originally developed in the context of turbulence [1–3]. Turbulence is also highly relevant beyond theoretical physics, playing an important role in applied areas such as mixing technology and meteorology.

While inertial turbulence is governed by the Reynolds number and arises when inertial forces dominate over viscous forces, turbulent-like behaviour has also been observed in bacterial suspensions at very low Reynolds numbers [4]. Since this discovery, significant effort has gone into defining this new class of turbulence, known as active turbulence [5]. More recent studies reveal the existence of yet another turbulent regime, characterized by labyrinthine patterns and dynamical arrest [6].

This is where the present thesis attempts to contribute by providing a study of mixing in these flows, something that has not been done before. To this end, we have divided the thesis into three sections. The first introduces the model of defect-free active nematics that exhibit turbulent behaviour and reviews the literature on mixing and the advection of tracer particles. The second section forms the core of this work, where we explain the simulations carried out, their analysis, and the results obtained. We describe in detail the observables constructed to characterize the different regimes of active turbulence, and examine the insights they provide into the behaviour of the flow. Among these observables are the ballistic time and the loyalty time, which help quantify transport properties. In addition, we include other noteworthy results, such as the clustering and particle caustic formation, which are not based on an observable but offer valuable information for understanding the different features of transport in each flow regime. Finally, the conclusions summarise our progress in understanding the field, as well as outlining possible future research directions.

A. Introduction to active turbulence

Over the past two decades, active fluids have emerged as a new paradigm in non-equilibrium statistical physics. They are a continuous medium driven internally dissipating energy, and therefore generating spontaneous flows and forces. It has been shown that, for a range of parameters, these flows become chaotic and show turbulent-like behaviour [5]. Since active fluids operate at very low Reynolds number, inertia is not what is driving the chaotic flow but, still, the flow is reminiscent of classic inertial turbulence (there is a universal scaling of the en-

* edejuabi7@ub.edu
† master.complex.biophys@ub.edu

ergy spectrum predicted first by Giomi [7] and numerically found in [8]). Instead, in active fluids, what induces turbulence in the flow is the dissipation of energy of its constituents, which is the so-called activity.

There are some important differences from the classical inertial turbulence. Perhaps the most important one is the lack of energy cascades, and that the scale at which energy is injected is not imposed by the external driving as an input, but rather, it is the active fluid that self-organizes. This means that the scale at which energy is injected is, in fact, part of the solution. On the other hand, the velocity power spectrum of active nematic turbulence features a scaling law of -1 for large scales, which is independent of the material properties and the appearance of topological defects. This universal behaviour is what may suggest that we may be in front of a new class of turbulence that the literature calls active turbulence [5]. To what extent active chaotic flows define a new class of turbulence has to be settled yet, but these chaotic flows have already been found in many different experimental realisations: bacterial suspensions [9], swarming sperm [10], mixtures of cytoskeletal components [11], tissue cell monolayers [12], and artificial self-propelled particles [13]... To study these systems, we will restrict ourselves to the defect-free active nematic turbulence, which makes the simulations less demanding, and if we wanted to test our model experimentally, we would use a microtubule-kinesin suspension in two dimensions because it has the same symmetries as our defect-free active nematic model for the labyrinthine case.

Finally, discoveries show flow's behaviours that rarely, if ever, have been seen: unicursal labyrinth-like patterns with an arrested dynamics [6]. Now we will define the model with which we can simulate the flows mentioned above, which at the same time will provide the velocity fields responsible for the advection of particles and the passive scalar.

1. *Hydrodynamics of defect-free active nematics*

We build our model of the hydrodynamics of defect-free active nematics from a phenomenological perspective and rely on symmetries and conservation laws. This way we are coarse-graining the fast variables and studying how the hydrodynamic modes and the order parameters, associated with breaking symmetries, evolve.

We will also consider the modulus of the nematic vector n_α to have a fixed modulus $n_\alpha n_\alpha = 1$, which implies we can describe the nematic vector field with just an angle field θ that ranges from 0 to 2π, if the fluid is polar, or from 0 to π, if nematic, and ensure there are no topological defects.

To build the dynamic equations of our variables, we start from the momentum conservation law and the dynamics of the director field from passive nematics. After some involved calculations that we summarize in the appendix section we reach these equations for the stream function of the flow ψ, defined by $v_x = \partial_y\psi$ and $v_y = -\partial_x\psi$, and the nematic director angle θ, defined as $\mathbf{n} = (\cos\theta, \sin\theta)$:

$$\begin{aligned}\nabla^2\omega = \nabla^4\psi = &-S\partial_\alpha\partial_\beta\bar{q}_{\alpha\beta}\\ &+R\nu\partial_\alpha\partial_\beta(\bar{q}_{\alpha\beta}h_\parallel - q_{\alpha\beta}h_\perp)\\ &+\frac{R}{2}\nabla^2 h_\perp + R\epsilon_{\alpha\beta}(\partial_\alpha h_\parallel)\partial_\beta\theta,\end{aligned} \tag{1}$$

$$\partial_t\theta - \epsilon_{\alpha\beta}\partial_\alpha\psi\,\partial_\beta\theta + \frac{1}{2}\nabla^2\psi = h_\perp + \nu q_{\alpha\beta}\partial_\alpha\partial_\beta\psi. \tag{2}$$

The first thing to comment is that we have made the equations dimensionless with the system size L, rescaling time by the active time $\tau_a = \eta/|\zeta|$, pressure by the active stress $|\zeta|$ and the orientational field by K/L^2, where K is the constant in the approximated Frank free energy coming from the liquid crystals theory. Our equations have some dimensionless parameters that we can tune to reach the flow regime we want. The flow activity is represented by the parameter $A = L^2/l_a^2$, where $l_a^2 = K/(|\zeta|R)$ is the active length. $R = \gamma/\eta$ is a viscosity ratio and S is the sign of the active stresses $S = \text{sign}(\zeta)$. Thus, for extensile stresses, S would be positive, and for contractile stresses, negative. Besides, it can be easily checked that the dynamics is invariant under the transformation $\nu \to -\nu$, $S \to -S$ and $\theta \to \theta \pm \pi/2$. However, the hydrodynamics changes dramatically in the change of sign of the product of S and the flow alignment coefficient ν [6], where $\nu \leq 0$ corresponds to rod-like nematic components and $\nu > 0$ corresponds to disk-like.

Less important for a first view of the defect-free active nematics model are the nematic orientation tensor $q_{\alpha\beta} = n_\alpha n_\beta - 1/2\delta_{\alpha\beta}$ and its anti-symmetrized version $\bar{q}_{\alpha\beta} \equiv -\epsilon_{\alpha\gamma}q_{\gamma\beta}$. We are also defining the parallel and the perpendicular component of the orientational field as [14]:

$$h_\perp = \frac{1}{A}\nabla^2\theta, \quad h_\parallel = \nu\bar{q}_{\alpha\beta}\partial_\alpha\partial_\beta\psi. \tag{3}$$

The second thing to realize, and more importantly, is that the stream function is entirely determined by the director angle by equation (1). Therefore, fixing the director norm leaves the whole problem to a single degree of freedom: the director angle θ. This makes simulating this model much simpler than others, enabling larger sizes and times to be reached. Besides, by precluding topological defects, the problem has a biunivocal correspondence to the polar active fluids.

2. *Labyrinths vs chaotic flows*

To finish this introduction in active turbulence, we take a closer look at the two different scenarios depending on the sign of the product of $S\nu$. The case in which $S\nu > 1$ corresponds to strong large-scale turbulence:

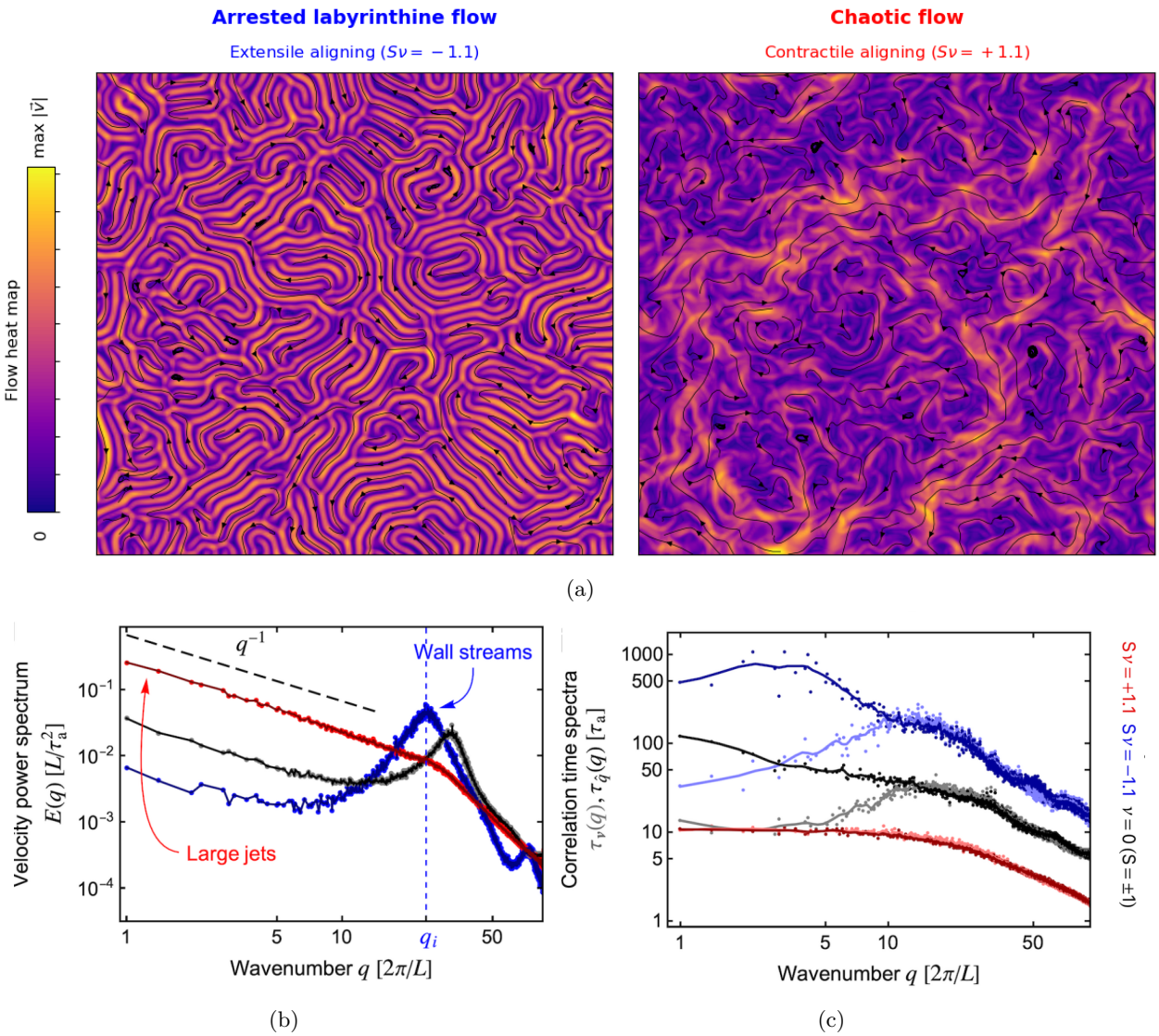

FIG. 1: **(a):** Snapshots from simulations of our model of defect-free active nematic turbulence in the two regimes according to the flow alignment, fixing the sign of the active stress to $S = -1$. **(b):** Velocity power spectra characterizing fully developed active nematic turbulence for the chaotic (red) and the labyrinthine (blue) case, and an intermediate case ($\nu = 0$ in black). We see the large jets of the chaotic regime and the selected wavelength corresponding to the wall streams. All three cases follow the universal -1 scaling law expected for big scales. **(c):** The correlation time spectra of the velocity field and the nematic field show much larger correlation times for the labyrinthine regime than for the chaotic case. Panels (a) and (b) adapted from reference [6].

chaotic flows with transient large-scale jets, as is shown in the kinetic energy spectrum in Figure 1b. The flow patterns are largely uncorrelated with the director field and are produced by long-range hydrodynamic interactions. We will call these the chaotic flows, which reveal some statistical similarities to inertial turbulence, such as the flow field with vortices at many scales and the short correlation times at all length scales, as Figure 1c shows. Nevertheless, this turbulent flow still presents a typical length scale at which wall patterns form and break continuously because they are unstable [14].

On the other hand, in [6] it is shown that the case in which the product is negative, $S\nu < 1$, corresponds to a flow in which dynamics seems to have been arrested and the extraordinary labyrinth-like patterns arise. Unlike the $S\nu > 1$ case, the wall patterns at the typical length scale are stable, but with a non-relaxational dynamics in the sense that there is still a weak background of large-scale chaotic flows producing the -1 scaling law. This resembles the systems displaying frustration like gels and glasses with long correlation times, and tends towards a state in which walls form a unicursal labyrinth.

Another important point to highlight is the formation of labyrinthine flows in real active fluids, such as micro-

tubule–kinesin suspensions. Although the current model assumes the absence of topological defects, efforts are underway to incorporate defects into the model. Preliminary results suggest that labyrinth patterns persist when the defect density remains low.

B. Introduction to mixing

This work focuses on mixing within a novel class of turbulent flows. To proceed, we must first understand the concept of mixing and how it can reveal properties of the underlying advective velocity field.

The science of mixing studies the evolution of a system from one state of simplicity, where the constituents of the system are segregated, to another state of simplicity: uniformity [15]. Therefore, a substance is said to be properly mixed if gradients are lowered down to the interparticle scale. There are mechanisms, like advection by a turbulent flow, that may speed up the evolution towards complete uniformity, but it is diffusion alone that drives the system to this final state of simplicity down to the intermolecular scale. Therefore, the equation giving the evolution of the system is the advection-diffusion equation:

$$\partial_t c = D\nabla^2 c - \mathbf{v}\cdot\nabla c, \tag{4}$$

where $c(t,\mathbf{r})$ is the concentration field of a passive scalar, D is the diffusion constant, and $\mathbf{v}$ is the incompressible velocity field that advects the passive scalar.

Even though the advective term can dominate over the diffusion one, diffusion has a singular role, and advection only speeds up the evolution towards uniformity. This can be understood easily with the time evolution of the fluctuations around the mean concentration, also called *mixing rate* [16]:

$$\frac{d}{dt}(\langle c^2\rangle - \langle c\rangle^2) = -2D\langle(\nabla c)^2\rangle, \tag{5}$$

which shows that fluctuations in concentration decay only due to diffusion. Then, the role of advection is to deform the concentration field towards lower scales, where diffusion is more efficient, as can be checked with the Fourier transform of the diffusion equation:

$$\partial_t \hat{c} = -Dq^2\hat{c}. \tag{6}$$

All this implies that mixing is neither stirring nor blending, and so the limit $D = 0$ is a singular one. Nevertheless, we are interested in this limit because it provides the greatest amount of information about advective flow and its transport properties. We can do this by simulating the advection of tracer particles without diffusion. But then, it is important to keep in mind that in that case, we are not studying mixing, although we can build useful observables with a coarse-grained particle density field.

1. *Designing observables*

When studying the mixing of a substance, we need to consider the observables that can best answer our questions. Usually, it is not the mean concentration of the mixture $\langle c\rangle$ nor the variance $\langle c^2\rangle - \langle c\rangle^2$ that we are interested in, but the extreme events and their probability to happen. We may also want to ask the time it takes to reach the mixed state, which comes from an interplay between the advective flow and the strength of diffusion, or, more related to our work, the transport properties the flow has, especially in the limit when diffusion is greatly inefficient.

Therefore, to obtain the probability of an extreme concentration event, we can rely directly on the **probability density function of the concentration of the mixture** $p(c)$, which defines de probability of finding the mixture between concentrations c and $c + dc$ and is well normalized $\int p(c)dc = 1$. The notation $\langle\cdot\rangle$ defines the average of an observable weighted by $p(c)$. It is shown to evolve from the initial state to the complete uniformity $p(c) = \delta(c - \langle c\rangle)$ with a gamma function whenever we have confined conditions that force the strips of the dispersing mixture to overlap [15].

To study the transport properties, instead of the probability density function, we may prefer to use the concentration field itself and its spatial distribution. Then, for instance, we will use $\overline{r^2}$ to define the **spatial second moment** of the concentration field, where the concentration field will always fulfil $\int c(\mathbf{r},t)d^2r = 1$. This observable is equivalent to the **mean squared displacement** of the tracer particles and will be useful to study the transport properties of the flow. We can also compute the fourth moment $\overline{r^4}$ which will enable us to calculate the **excess kurtosis**:

$$\gamma(t) \equiv \frac{\overline{r^4}}{(\overline{r^2})^2} - 2, \tag{7}$$

which is 0 for a Gaussian statistics of independent displacements in two dimensions. For isotropic distributions, negative values of γ show that the distribution decays faster than a Gaussian, and when γ is positive, it exhibits heavy tails. Therefore, for these measures, we will use the tracer particles even though we are aware that this is not mixing in the strict sense discussed before.

II. SIMULATIONS AND THEIR ANALYSIS

The simulation of mixing and tracer particles in active flows was divided into two parts: advective flow simulation on the one hand, and simulation of mixing and tracer particles in the velocity field obtained on the other.

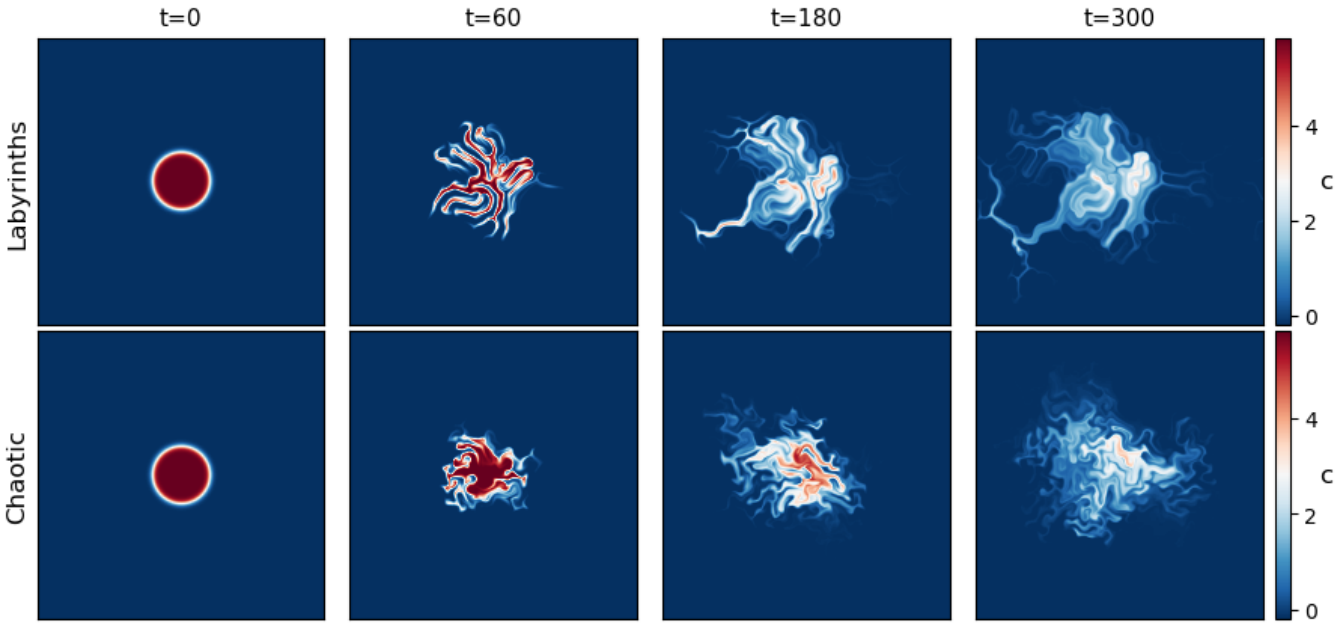

FIG. 2: Time evolution of the advection-diffusion of a passive scalar for the labyrinthine and chaotic flow. The diffusion constant is set to $D = 0.05$: the minimum value our spatial and temporal resolution allowed us.

A. Simulation of the active flow

The code, written in Julia, was provided by the supervisor, and I only had to implement minor changes for my purposes. When we wanted long recordings of the evolution of the velocity field, we used the faculty cluster to run the simulation. These simulations lasted for a couple of days.

The parameters used are the size of the system $L = 256$, which is a $2D$ plane with periodic boundary conditions, the activity number $A = 32 \cdot 10^5$, the sign of the active stress parameter $S = -1$ (contractile) and the the flow alignment coefficient negative $\nu = -1.1$ for the chaotic case, and positive $\nu = 1.1$ for the labyrinthine case.

The equations of the model (1) and (2) were solved with a program in Julia in the Fourier space when the flow alignment coefficient was $\nu = 0$. However, the cases in which $\nu \neq 0$ were computationally more demanding, and a finite-element program was used.

B. Simulation of the mixing

Once we have the velocity fields, we simulate the mixing of a passive scalar and the transport of tracer particles to describe the turbulent velocity fields.

1. *Simulation of the advection diffusion equation*

Mixing is studied through the advection diffusion equation (4), loading at every time step the velocity field from a previous simulation.

A code written in Julia working in the Fourier space was provided by the supervisor and modified to adapt to our needs. These simulations were computationally cheap and lasted no more than twenty minutes.

Since we wanted the low diffusion limit, we used diffusion constants from $D = 1$ down to $D = 0.05$, in units of the active length and active time. Figure 2 shows the evolution of the concentration field in four snapshots, for the chaotic and labyrinthine case.

2. *Simulation of the tracer particles*

This approach presents some crucial advantages over the simulation of the advection-diffusion equation. The first one is that the limit $D \to 0$ is very demanding for the simulations of the concentration field in terms of spatial and temporal resolution, but this limit can be achieved easily by simulating tracer particles that are advected by the velocity field. Thus, the equation to be solved for each particle is:

$$\dot{\mathbf{x}}(t) = \mathbf{v}(\mathbf{x}, t), \tag{8}$$

which is the Lagrangian description of the flow.

These simulations were done with a code written in C entirely on my own, and, like the advection-diffusion simulations, were cheap computationally, lasting for no

more than twenty minutes, for 10^5 particles. The integration method used was the Euler method, which is the least demanding computationally but also the least precise, with an error of the order of $\mathcal{O}(\Delta t^2)$. However, since we already had the limit of the updating of the velocity field every Δt, this precision is enough.

C. Results

The main objective in our study of mixing is the characterization of the two regimes of flows that we have called chaotic and labyrinthine.

Therefore, once we had run the simulations, I developed all the analysis programs in search of an observable able to:

1. Differentiate between the chaotic and labyrinthine regimes,
2. Capture the transport properties of each regime.

1. *Ballistic regime*

The first observable that could be used to do this is the mean squared displacement. We can compute it both as the spatial second moment of the concentration field and with the tracer particles. The advantage of the tracer particles is that we can get rid of the diffusive part and purely study the advection process.

We can see that the advection of the flow causes a ballistic transient that lasts the time during which the velocity field is correlated. However, the diffusive term in the advection-diffusion equation (4) tends to suppress this ballistic transient. So, if we want to study the velocity field and not just a diffusion problem, we must take the limit $D \to 0$. We can explicitly see this from the formula derived for the mean squared displacement in the appendix section:

$$\overline{r^2} = 4Dt + 2\int_0^t dt \int_A \mathbf{v}\cdot\mathbf{r}\; c(\mathbf{r},t)d^2r, \tag{9}$$

where A is the area of the system. If we now perform a Taylor expansion for small times, we obtain:

$$\overline{r^2} = 4Dt + \frac{t^2}{\sigma^2}\int_A (\mathbf{v}\cdot\mathbf{r})^2 c(\mathbf{r})|_{t=0} d^2r + \mathcal{O}(t^3), \tag{10}$$

where the initial concentration profile is assumed to be Gaussian with σ^2 spatial variance. This result contains the transient diffusive behaviour due only to the diffusive term and the second transient with ballistic behaviour only caused by the advection term, as Figure 3a shows. This final idea is valid regardless of the initial condition of the concentration profile, as soon as it has radial symmetry. Therefore, since the diffusion constant modifies the ballistic regime, we must use the tracer particle simulations to turn off diffusion and study the advective flow alone.

Once we have managed to remove the diffusive contribution by simulating the tracer particles, we analyse Figure 3b, which shows the mean squared displacement of the tracer particles without diffusion in the labyrinthine and chaotic case. We see the expected ballistic transients and realize that they last for different times in each case. We call this the ballistic time τ_b, which is around 50 for the labyrinths and 10 for the chaotic flow.

These ballistic times appear promising for our purpose of characterizing the two different flow regimes, and therefore, we must find a way to extract them quantitatively. To this end, we can express the mean squared displacement of the tracer particles in the following way, also derived in the appendix section:

$$\overline{r^2} = \langle|\mathbf{v}|^2\rangle \Delta t^2 \big(N + 2\sum_{i<j}^{N} g(i,j)\big), \tag{11}$$

where $\langle|\mathbf{v}|^2\rangle$ is the velocity of a step averaged over trajectories and Δt carry the time units of the discrete steps so that $t = \Delta t N$ and

$$g(\tau) = \frac{1}{\langle|\mathbf{v}|^2\rangle}\langle \mathbf{v}(\mathbf{s})\cdot\mathbf{v}(\mathbf{s}+\tau)\rangle \tag{12}$$

is the autocorrelation function of the velocity of a trajectory, which is only dependent on the difference of times because we are in a steady state regime.

Therefore, equation (11) already shows that the correlation of the velocities is closely related to the mean squared displacement, and so, as we expected, the ballistic time can be determined by the correlation of the velocities in the trajectory.

Before we get into the numbers to get the ballistic times, it will be helpful to understand the equation (11) better. If we take the limit in which the autocorrelation function is $g(\tau) = \delta(\tau)$, then the process is Markovian and we see that the mean squared displacement is diffusive (grows linearly with time) with an effective diffusion constant $D_{\text{eff}} = \langle|\mathbf{v}|^2\rangle\Delta t/4$. However, for short timescales, we can expect that the advective velocity field is correlated in time with an exponential decay characterized by τ_d. In this other case, we would have a short transient where we can approximate the exponential to a constant. This implies that the expression (11) takes the form of a ballistic term, proportional to N^2, while the diffusive terms proportional to N cancel out. Thus, we obtain the duration of the ballistic transient in the mean squared displacement by estimating the characteristic decay time of the autocorrelation function, which can also be defined as the average time the trajectory takes to change the initial direction. Figure 4 shows the autocorrelation of the velocities of the particles $g(t)$, and so the next step is to extract from them the decay time.

Firstly, the autocorrelation function of the chaotic case contains a lot of noise, so the best approach is to fit it to

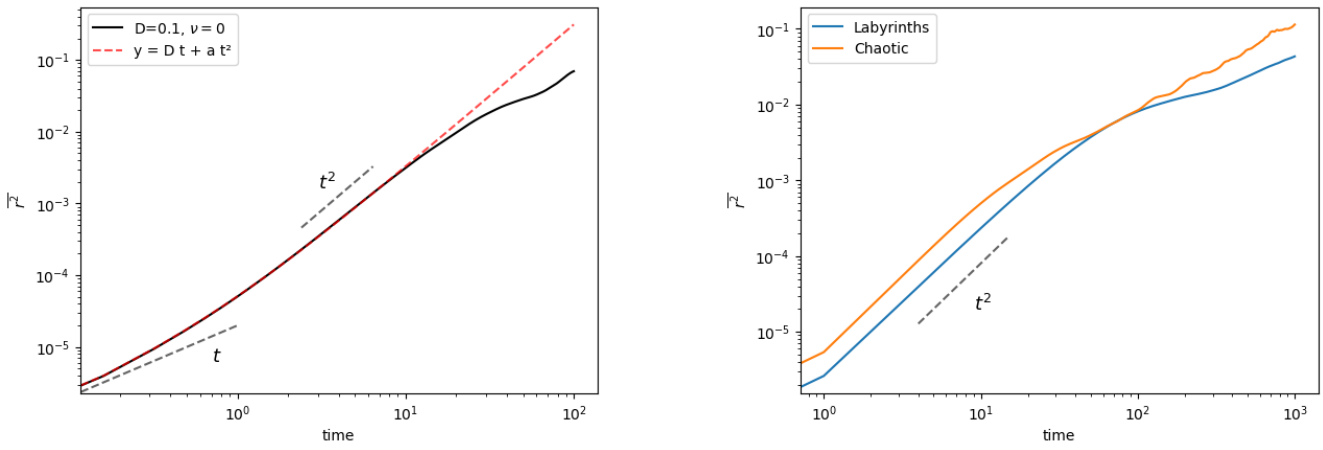

(a) (b)

FIG. 3: **(a):** mean squared displacement of the advection-diffusion simulation with flow alignment coefficient $\nu = 0$ and a diffusion constant $D = 0.1$. The ballistic correction of the diffusion limit is shown in red, matching perfectly the first transient of the curve. **(b):** mean squared displacement of tracer particles without diffusion for the labyrinthine case $\nu = 1.1$ and the chaotic case $\nu = -1.1$. The ballistic regime appears more clearly because we are at the $D = 0$ limit. Time is in active time units.

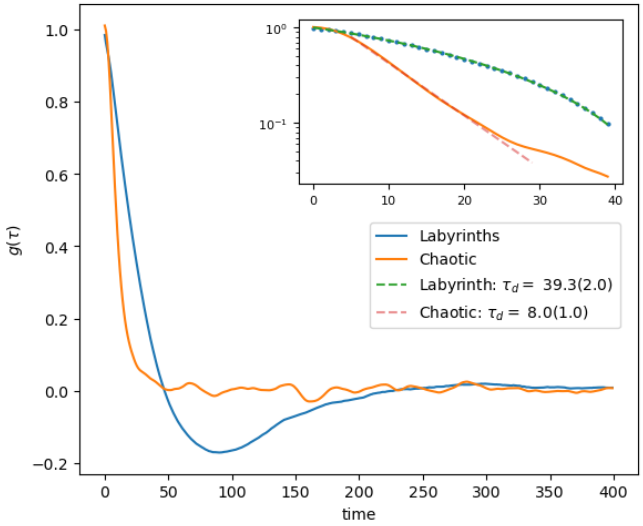

FIG. 4: Autocorrelation functions of the particle velocity computed with (12) for the labyrinthine and chaotic case. Inset: the first part of the autocorrelation functions, from which we can extract their decay times, and compare them to the ballistic times in the mean squared displacement. Time is in active time units.

an exponential function in the most appropriate region. This yields a characteristic decay time of $\tau_d = 8.0(1.0)$ for the chaotic case, which coincides with the duration of the ballistic regime in 3b.

By contrast, the labyrinth case exhibits an autocorrelation function with a very low noise level, but with a clear anti-correlation behaviour that cannot be explained by an exponential alone. To extract the decay time from the labyrinths' autocorrelation function, we found it necessary to fit the function $y = \exp(-t/\tau_d)\cos(\omega t)$, where the cosine tries to account for the anti-correlation displayed in 4. Thus, we obtain a decay time $\tau_d = 39.0(2.0)$ which also matches the ballistic time shown in 3b. The fitted value of ω is $\omega = 0.0335(10)$, which is of the same order as the inverse of the decay time. This shows that the cosine function is relevant for obtaining an accurate measurement of the decay time.

We cannot ignore the peculiar behavior of the correlation function in the labyrinth case, where the velocities of a trajectory do not simply decorrelate with time, as the exponential model suggests, but first anti-correlate. This is due to two things: first, the labyrinthine nature of the velocity field, and second, the dynamical arrest of the pattern flow. On one hand, particles follow the walls of the labyrinth, which has patterns where the wall turns 180° when it reaches a bifurcation, but this would not be enough to explain the anti-correlation if the labyrinthine pattern was not almost stationary. Previous work [6] has shown that the flow has an arrested dynamics with large correlation times 1c, and the patterns remain stable except for a weak background of large-scale chaotic flows displaying the universal -1 exponent shown in Figure 1b.

2. *Loyalty time*

One of the reasons mentioned before for the anti-correlation in Figure 4 is the dynamical arrest of the labyrinth flow. If the wall patterns changed shape in a shorter time scale, we would not see the anti-correlation regime. Thus, there is another time scale in the tra-

jectories that characterizes how the labyrinthine pattern decorrelates.

Following this direction, we can try to extract another characteristic time of the trajectories, because we see that the tracer particles in the labyrinths tend to follow the same paths, staying together even when turning. Thus, this second characteristic time will be larger than the ballistic time, and we will call it τ_L, the loyalty time. We suggested that it could be related to the timescale at which the labyrinthine pattern decorrelates, but in this work, we will not go so far, and we will just try to compute it from our trajectories. Nevertheless, we will see that it leads the way to one of the most significant differences between the chaotic flows and the labyrinths: clustering and caustics.

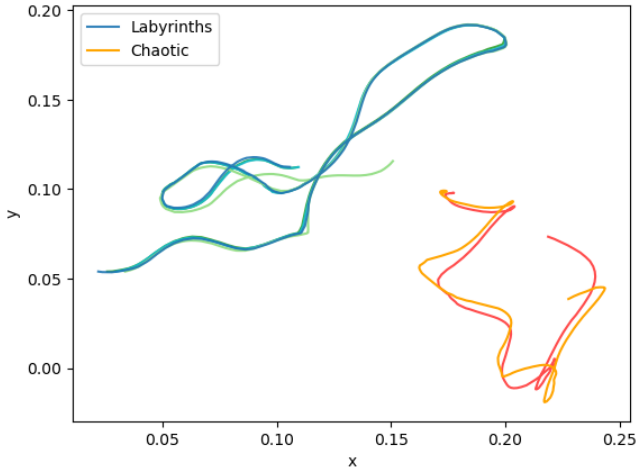

FIG. 5: Four particle trajectories of the labyrinthine case until $t = 300$ and two trajectories of the chaotic case until $t = 150$, initially very close together. We see that in both cases the ballistic time is shorter than the loyalty time: the particles stay close to each other even though they follow complicated trajectories, but in different ways and for different lengths of time.

We can attempt to extract this loyalty time τ_L by setting a threshold in distance and measuring the time that a pair of particles, initially together, separate more than the threshold. We find that the loyalty time is distributed according to an exponential probability function, and we can see in Figure 6 that the two regimes are very well differentiated and that they are one order of magnitude greater than their respective ballistic times. In the labyrinthine case, we can even see that some pairs of particles stayed together the whole simulation.

The choice of the threshold is only relevant if it can capture the time at which the trajectories separate and not just a fluctuation. This can be easily checked by visually analysing the trajectories. Our final choice of the threshold was the distance between walls, which corresponded to 10 times the initial separation of the particles.

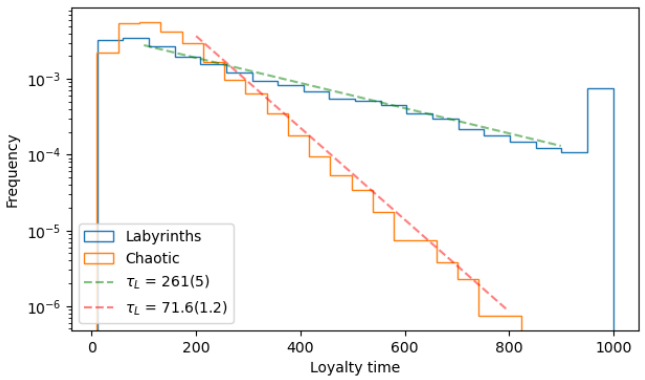

FIG. 6: Probability distribution of the loyalty time, in active time units, for the tracer particles in a labyrinthine flow and a chaotic flow, respectively.

3. *Clustering*

When computing the loyalty times of the particle trajectories, one could object that what makes the particles stick together is the fact that they are advected by the same flow jets and only separate when these jets can differentiate between the particles and advect them differently. This is what happens in the chaotic case, giving place to the parallel trajectories seen in Figure 5. The case of the trajectories in the labyrinths is different, though; traces are not merely parallel, but there is a tendency in the trajectories to coalesce. This is driving the particles to form clusters. To see it, we will now make a coarse-grained particle concentration field, and then use the probability distribution of the concentration.

We can construct this spatial distribution of particles and obtain the evolution of the probability of concentration distribution when we start from a uniform configuration of particles, corresponding to a Dirac delta probability distribution. To build it, we can either set the coarse factor to be the same as the velocity field resolution, or we can make it larger better to resolve the low-density region of the probability distribution. However, we must be aware that by doing this, we are losing statistics and the spatial correlations. Therefore, for Figures 7a and 7d, we chose the lowest velocity field resolution that still preserves the spatial patterns. For the probability distributions, we used a coarser resolution, four times lower, which helps us see the beginning of the distribution more clearly.

The distributions shown in Figures 7b and 7e settle into an attractor shaped like a gamma function as the flow drives the particles toward a statistically stationary state, which matches what is typically expected for mixing in a turbulent flow within a confined system [15]. However, there are clear qualitative differences between the chaotic case and the labyrinths, which can already be seen in the coarse-grained concentration fields in Figures 7a and 7d.

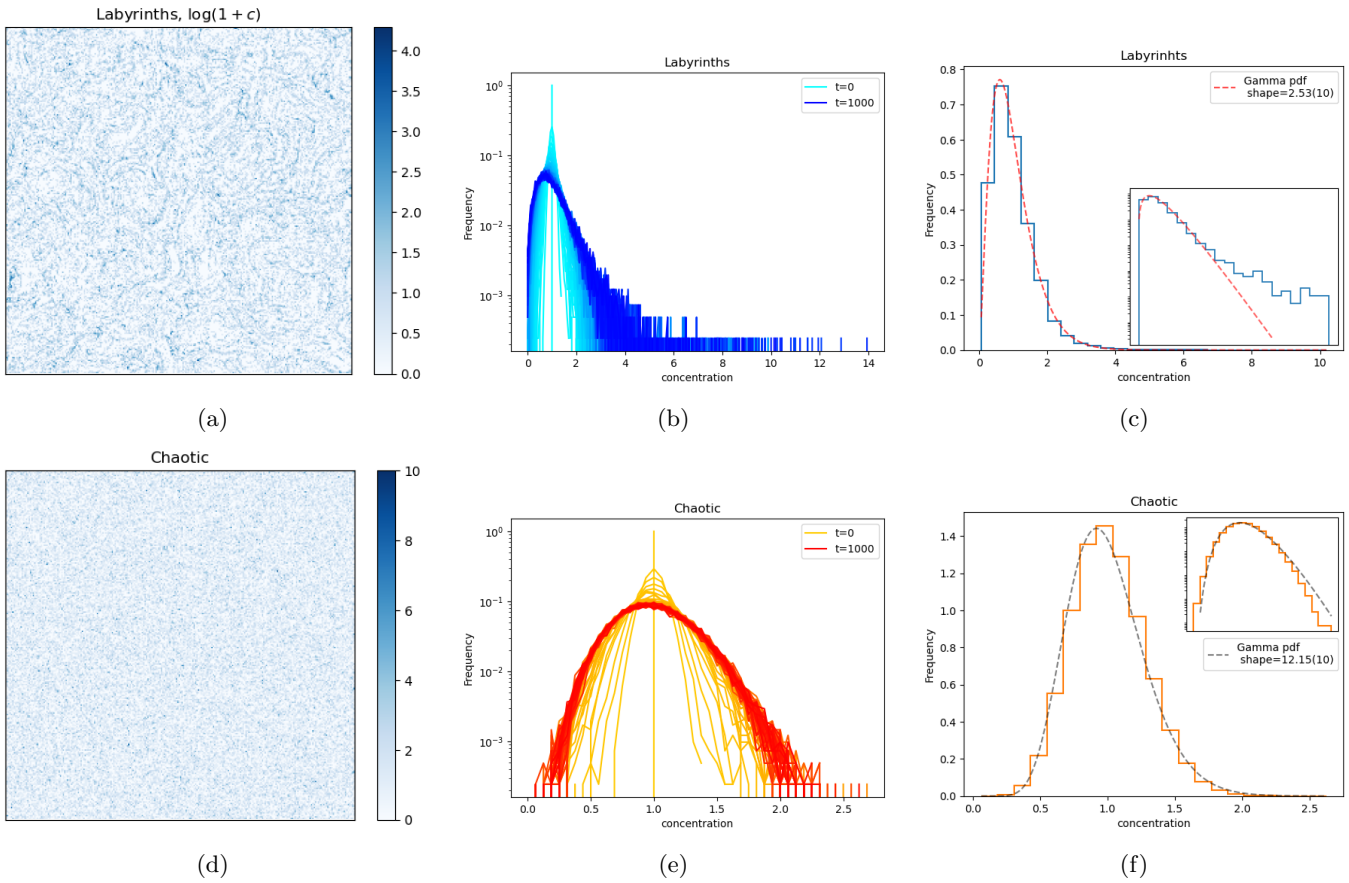

FIG. 7: **(a), (d):** Coarse-grained concentration field of the particles advected by the labyrinthine flow and the chaotic flow at the last time frame. We must use a logarithm to see the caustic patterns in the labyrinths because of the saturation of the particle clusters. The chaotic concentration field is much more homogeneous. **(b), (e):** Time evolution of the coarse-grained concentration of particles PDF of both cases. We start from a homogeneous state, and the distribution approaches a gamma distribution, but in the labyrinthine case, it takes longer and has long tails. **(c), (f):** Concentration distributions averaged over the stationary state frames. The main body fits very well to a gamma distribution in both cases, but the labyrinths present heavy tails. The tail behaviours are explicitly checked in the insets, where lin-log scales are used.

The first key difference is that in the labyrinthine flows, particle clustering leads to a concentration field with long tails, clearly deviating from the gamma-like behaviour. In contrast, the concentration field in the chaotic case fits a gamma function very well. This suggests that labyrinthine flows are not typical turbulent flows that mix tracers evenly and in an uncorrelated way. Instead, tracer particles in these flows tend to cluster and form caustics, even in the limit of zero inertia, which is our case. It would be interesting to explore this behaviour further in the context of other known caustic phenomena [17].

We also observe that the time it takes to reach the attractor differs between chaotic and labyrinthine flows. To investigate this, we look at how the second moment of the particle concentration distribution evolves. Once again, the dynamics of the labyrinthine flow are much slower than those of the chaotic flow, resembling the behaviour seen in glasses and gels. One could question whether the concentration distribution in the labyrinths has truly reached a stationary state. Although Figure 7b suggests that the main part of the distribution has settled into the gamma attractor, the standard deviation continues to grow, likely due to the ongoing formation and growth of particle clusters.

4. Other observables

We believe that the observables we have developed, such as the ballistic time and the loyalty time, as well as the clustering and caustic properties studied with the coarse-grained concentration field, characterize very well the different regimes of active turbulence we are considering. However, in our search for the best observable, we came across others that may also deserve a word. In

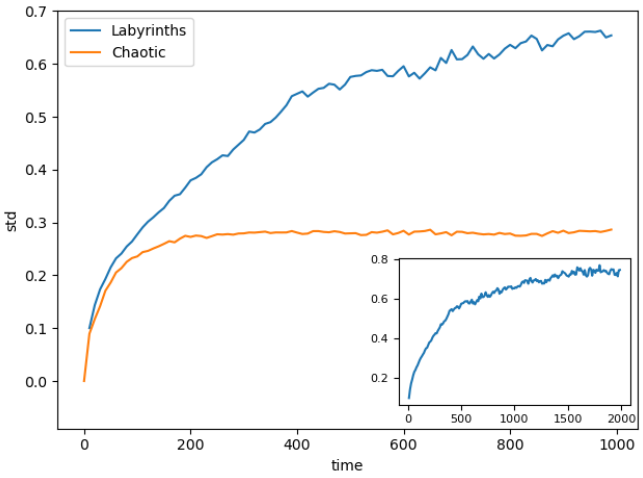

FIG. 8: Time evolution of the standard deviation of the particle concentration distribution of each case. We see that in the chaotic flow, a steady state is reached in the first 200 steps, while in the labyrinths the standard deviations evolve very slowly, and we needed to double the simulation to reach a steady state in 1500 active time units.

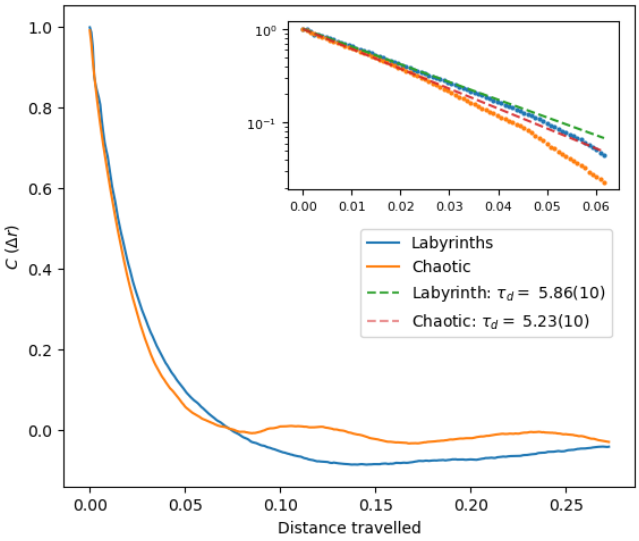

FIG. 9: Distance correlation of the velocity of trajectories. Fitting exponentials yields the persistence lengths of the trajectories. Distances are in the length of the system units.

this way, we aim to illustrate the unusual nature of the labyrinthine flows and how they can enable an efficient mixing with unique properties.

First of all, for the sake of completeness, we can compute the persistence length of the trajectories of the tracer particles. This measure is related to the autocorrelation of the velocity $g(t)$ that we have already studied, but with the difference that it is not the correlation in time, but along the length covered. Therefore, instead of the characteristic time τ_d that we related to the ballistic time, we obtain a characteristic length called the **persistence length**. The calculation to obtain the new correlation function is:

$$C(\Delta r) = \frac{1}{\langle |\mathbf{v}|^2 \rangle} \langle \mathbf{v}(\mathbf{s}) \cdot \mathbf{v}(\mathbf{s} + \mathbf{\Delta r}) \rangle, \tag{13}$$

where, unlike (12), we are not discretizing the trajectory by equidistant time intervals, but by length intervals.

In Figure 9 we see that the correlation function in distance is very similar to the one in time, Figure 4, so we observe the same anti-correlation regime in the labyrinths. However, we obtain very similar persistence lengths: $p = 5.86(10)$ for the labyrinths and $p = 5.23(10)$ in the chaotic case. This result highlights that the mean velocity of the chaotic flow is larger than that of the labyrinths, so we must be careful when comparing the flows. However, this result can tell us that the labyrinths are more efficient at transporting, because they can cover the same distance ballistically with less kinetic energy.

In this respect, perhaps the most direct way of differentiating the ballistic transport by each regime is the **radial distribution of the concentration field**. Simulations of the advection-diffusion equation lead to different concentration fields depending on the advective flow we use. From the time frames 2, we can see that the labyrinthine flow was very efficient in transporting matter through its labyrinth paths, carrying matter far away from the initial position. On the other hand, the chaotic flow was not so efficient at short time scales, but its conventional turbulent behaviour shows that it enhances mixing more than the labyrinths at longer timescales. This is what the evolution of the radial profile of the concentration field can show very clearly, as displayed in 10. The radial profile is calculated by fixing the distance to the origin, averaging over the polar angle, and multiplying by the Jacobian of the polar coordinates.

Therefore, what we see is that, in the labyrinthine case, matter is transported far away from the origin in a very short time, but in the end, it is outperformed by the chaotic flow. We can realize that this behaviour is already present in the mean squared displacement of the particles 3b, which is nothing but the second spatial moment of the concentration field.

Finally, we may ask whether the system reaches a diffusive regime after the initial ballistic transient. The mean squared displacement shown in Figure 3b hints at a power-law behaviour at long times. Still, with our current data, we cannot decide for or against, nor extract the power exponent and verify it grows linearly, i.e., it is diffusive. Instead, we can use the **excess kurtosis** γ defined as (7) to at least test that the system has *not* reached the diffusive regime [18]. Since γ quantifies deviations from Gaussian displacement statistics, a non-zero

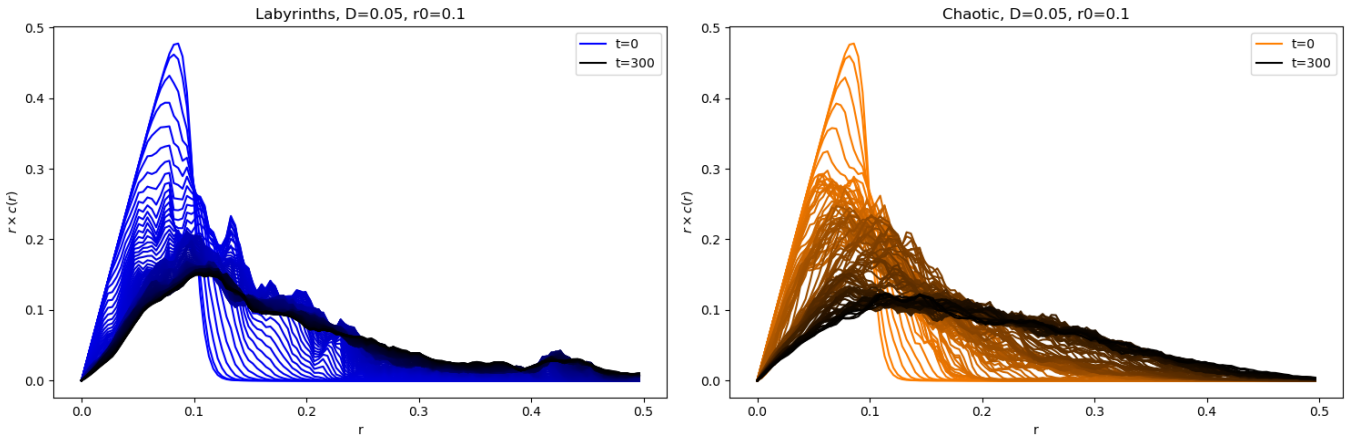

FIG. 10: Time evolution of the radial profile of the advection-diffusion equation for the labyrinthine and chaotic flow, respectively. The diffusion constant is set to $D = 0.05$, the minimum value our spatial and temporal resolution allowed us. We see that the chaotic flow moves toward a homogenous state more rapidly, but the labyrinthine flow can transport matter far from the origin very efficiently through its labyrinthine paths.

value indicates non-diffusive behaviour. Figure 11 shows that the chaotic case presents an excess kurtosis around 0, so we cannot decide whether we have reached a diffusive limit. However, the labyrinths have $\gamma > 0$, meaning the displacement distribution has long tails. Therefore, we can be sure we are not in a diffusive regime. Furthermore, when we extend the simulation by doubling its time, the labyrinthic case shows that it does not decay to zero but reaches a steady state value of around 0.8 after 1500 time steps. Further statistics would be useful for computing this value precisely. Interestingly, this evolution of $\gamma(t)$ resembles the one in the run-and-tumble dynamics followed by bacterial swimmers [18] with the difference that we do not reach a diffusive limit, since $\gamma(t)$ does not go to zero.

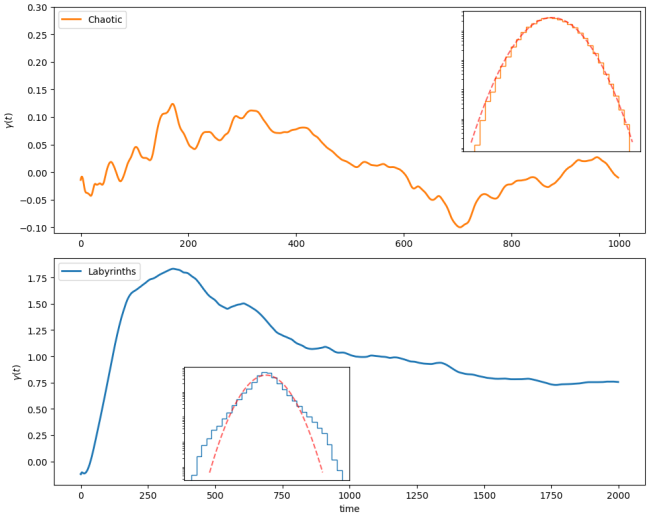

FIG. 11: Excess kurtosis function $\gamma(t)$ for the displacement distribution as a function of time. While the chaotic case does not present significant deviations of the kurtosis from a Gaussian distribution, the labyrinths present positive γ that imply a long-tailed distribution of displacements. The insets, in lin-log scale, help to visualize the deviations from the Gaussian of the distributions of x displacements after 400 time steps.

III. CONCLUSIONS

The emergence of turbulent-like flows in active fluids is a surprising phenomenon that continues to be the subject of research. Perhaps even more unexpected is the discovery of labyrinthine flows, characterized by their unicursal structure and arrested dynamics, which make them fundamentally different from conventional turbulence. This thesis has contributed to our understanding of these labyrinthine flows by providing a study of mixing that identifies the key properties that distinguish them from the chaotic case examined here, with $S\nu > 1$. This latter case can be considered a more standard turbulent regime. In doing so, we have achieved our goal of constructing observables capable of distinguishing between these flow regimes and capturing their distinct transport behaviours.

Among these observables, we can start by commenting on the ballistic time, which is the period during which the trajectories in each flow are advected in a ballistic way. We have seen that this time is larger for the labyrinth flow, $\tau_b = 39.3(2.0)$, than for the chaotic, $\tau_b = 8.0(1.0)$, where we have used the characteristic time of the autocorrelation function (12) to compute them. This ballistic behaviour is also shown in the time evolution of the radial profile 10 of the concentration field 2.

After this ballistic transient, the mean squared displacement alone 3b cannot test whether we have reached the diffusive limit or not, so we use the excess kurtosis

$\gamma(t)$ to see that the distribution of displacements of the labyrinths has long tails and so deviates strongly from a Gaussian, decaying very slowly with time. Moreover, we know from the anti-correlation region of the labyrinth in Figure 4 that the state after the ballistic transient may be more complicated than a power law. In contrast with the labyrinths, the chaotic case presents a $\gamma(t)$ fluctuating around zero compatible with a Gaussian distribution. We need improved statistics of its mean squared displacement to check whether we reach a diffusive limit.

By analysing the trajectories of tracer particles, we observed that particles starting close together tend to remain close, even while following complex paths. This behaviour differs both quantitatively and qualitatively between the labyrinthine and chaotic cases. To capture the quantitative difference, we used the loyalty time, which was $\tau_L = 261(5)$ for the labyrinths and $\tau_L = 71.6(1.2)$ for the chaotic case. To study the qualitative difference, we used the coarse-grained concentration of particles. The probability distribution of the concentration of particles had different behaviours for each case: in both cases, the main body of the distribution followed a gamma function, as expected in [15], but the labyrinth case had a heavy tail, showing important clustering effects. Besides, while the coarse-grained concentration of the chaotic case was spatially uncorrelated, in the labyrinth case, patterns emerged, suggesting particle caustics.

Therefore, our work does not exhaust the field of study of mixing in labyrinths in active turbulence but rather opens up new research directions. For instance, improved statistics and longer simulations would be valuable for determining whether these flows ultimately reach a diffusive regime and whether the clustering of particles truly settles into a stationary state. We also leave for future research the study of topological defects in the nematic vector field, which we suspect could drive the system toward a melted phase, as well as a study of mixing deep into the stationary state. Finally, another important line of study is the formation of particle caustics in labyrinthine flows. It is a legitimate question to ask whether these caustics influence the emergence of labyrinths when we consider the components of the active fluid as the true tracers of the flows they generate.

APPENDIX

A. Hydrodynamic model

A priori, in our defect-free active nematic model, we have 6 hydrodynamic variables: mass density, energy density, momentum density (a two-dimensional vector), and the polarization field or nematic vector n_α, which comes from the spontaneous breaking of the spatial symmetry. We will consider the modulus of the nematic vector n_α to be a fast variable and so fix it to $n_\alpha n_\alpha = 1$. This implies we can describe the nematic vector field with just an angle field θ that ranges from 0 to 2π if the fluid is polar or from 0 to π if nematic.

To build the dynamic equations of our variables, we start from the momentum conservation law and the dynamics of the director field from passive nematics. The momentum conservation law reduces to force balance because we are at a low Reynolds number, where η and γ are the shear and rotational viscosities, respectively.

$$0 = -\partial_\alpha P + \partial_\beta(\sigma_{\alpha\beta} + \sigma^a_{\alpha\beta} + \sigma^E_{\alpha\beta}), \tag{14}$$

$$\partial_t n_\alpha + v_\alpha \partial_\beta n_\alpha + \omega_{\alpha\beta} n_\beta = \frac{1}{\gamma} h_\alpha - \nu v_{\alpha\beta} n_\beta. \tag{15}$$

The incompressibility condition of the flow field $\partial_\alpha v_\alpha = 0$ is enforced by the pressure P term; $\sigma^E_{\alpha\beta}$ is the Ericksen stress and the $\sigma_{\alpha\beta}$ and $\sigma^a_{\alpha\beta}$ are the symmetric and antisymmetric parts of the deviatoric stress tensor:

$$\sigma^a_{\alpha\beta} = \frac{1}{2}(n_\alpha h_\beta - h_\alpha n_\beta), \quad \sigma^E_{\alpha\beta} = -\frac{\delta F_n}{\delta(\partial_\alpha n_\gamma)} \partial_\beta n_\gamma, \tag{16}$$

$$\sigma_{\alpha\beta} = 2\eta v_{\alpha\beta} - \zeta q_{\alpha\beta} + \frac{\nu}{2}(n_\alpha h_\beta + h_\alpha n_\beta - n_\gamma h_\gamma \delta_{\alpha\beta}). \tag{17}$$

We are using $h_\alpha = -\delta F_n / \delta n_\alpha = K\nabla^2 n_\alpha + h^0_\parallel n_\alpha$ for the orientational field produced by the distortions in the nematic vector $\mathbf{n}$. Besides, in the one constant K approximation, the Frank free energy reads:

$$F_n = \int \left[\frac{K}{2}(\partial_\alpha n_\beta)(\partial_\alpha n_\beta) - \frac{1}{2} h^0_\parallel n_\alpha n_\alpha \right] d^2 r \tag{18}$$

where we are assuming that deep in the nematic phase the director field has fixed modulus and, thus, we are impeding topological defects using the Lagrange multiplier $h^0_\parallel$.

In the constitutive equation (17) we are using η as the shear viscosity; $v_{\alpha\beta} = 1/2(\partial_\alpha v_\beta + \partial_\beta v_\alpha)$ stands for the symmetric part of the strain rate tensor; we are using ζ as the active stress parameter and $q_{\alpha\beta} = n_\alpha n_\beta - 1/2\delta_{\alpha\beta}$ stands for the nematic orientation tensor defined by the director field $\mathbf{n}$. The flow alignment parameter is ν and describes how the stresses arise due to flow alignment: $\nu \leq 0$ corresponds to rod-like nematic components, while $\nu > 0$ corresponds to disk-like.

On the other hand, equation (15) determines the dynamics of the nematic field. The left hand side is the co-rotational and co-moving material derivative of the director field and so $\omega_{\alpha\beta} = 1/2(\partial_\alpha v_\beta - \partial_\beta v_\alpha)$ is the vorticity tensor, while in the right hand side we have the dissipative terms: the elastic torques acting on the director field, done by the orientational field h_α and the reorientation due to the flow-alignment effect.

When it comes to simulate the evolution of the active fluid given by (14) and (15), we can reduce the degrees of freedom to the stream function ψ defined by $v_x = \partial_y \psi$ and $v_y = -\partial_x \psi$, and the nematic director

angle θ: $\mathbf{n} = (\cos\theta, \sin\theta)$. We make the equations dimensionless with the system size L, rescaling time by the active time $\tau_a = \eta/|\zeta|$, pressure by the active stress $|\zeta|$ and the orientational field by K/L^2, and finally reach the equations (1) and (2) of the evolution of the stream function and the nematic angle. For the definition of $\bar{q}_{\alpha\beta} \equiv -\epsilon_{\alpha\gamma} q_{\gamma\beta}$ we are using the Levy-Civita pseudotensor $\epsilon_{\alpha\beta}$.

B. Concentration field approach of the MSD

In the concentration field approach, the mean squared displacement is calculated as the spatial second moment of the concentration field in time: $\overline{r^2}(t) = \int_A r^2 c(\mathbf{r}, t) d^2$, where the concentration field fulfils $\int_A c(\mathbf{r}, t) d^2 r = 1$. We can obtain the time evolution of the mean squared displacement (9) from the advection diffusion equation (4) by multiplying by r^2 and integrating over the area of the system, which we consider to be infinite, or with periodic boundary conditions:

$$\partial_t \overline{r^2} = D \int_A \nabla^2 c(\mathbf{r}, t) r^2 d^2 r - \int_A \mathbf{v} \cdot \nabla c(\mathbf{r}, t) r^2 d^2 r. \quad (19)$$

The diffusive term can be rewritten using the polar form of the Laplacian operator, and so it reduces to

$$\begin{aligned} D \int_A \nabla^2 c(\mathbf{r}) r^2 d^2 r &= D \int_0^\infty dr \int_0^{2\pi} d\theta r^2 \partial_r (r \partial_r c) + r \partial_\theta^2 c \\ &= 4D, \end{aligned}$$

because the integral of the concentration is conserved, and this identity $\partial_\theta c(r, \theta = 2\pi) = \partial_\theta c(r, \theta = 0)$ is fulfilled by continuity.

On the other hand, the advective term can be managed so that it also simplifies to just one term:

$$\begin{aligned} \int_A \mathbf{v} \cdot \nabla c \; r^2 d^2 r &= \int_A \nabla (r^2 \mathbf{v} c) d^2 r - \int_A \nabla (r^2 \mathbf{v}) c \; d^2 r \\ &= 0 - \int_A \nabla (r^2) \cdot \mathbf{v} c \; d^2 r \\ &= -2 \int_A \mathbf{r} \cdot \mathbf{v} c \; d^2 r. \end{aligned}$$

After performing the integration by parts, we see that the first integral vanishes on the boundaries, the second yields only the gradient of r^2, because the flow is incompressible, leading to the final expression.

Therefore, we can integrate the differential equation (19) and we end up with the expression (9) with a diffusive term and an additional term coming from the advection by the flow:

$$\overline{r^2} = 4Dt + 2 \int_0^t dt \int_A \mathbf{v} \cdot \mathbf{r} \; c(\mathbf{r}, t) d^2 r.$$

This expression for the evolution of the mean squared displacement is exact and involves no approximation or premise.

However, to better understand this advective term, we will assume the initial condition of the concentration field to be radially symmetric, and more specifically, Gaussian with spatial variance σ^2. If we now make a Taylor expansion of the integral up to second order, we obtain:

$$\begin{aligned} \int_0^t dt \int_A \mathbf{v} \cdot \mathbf{r} c \; d^2 r = t \int_A \mathbf{v} \cdot \mathbf{r} c \; d^2 r|_{t=0} + \\ + t^2 \frac{1}{2} \partial_t \int_A \mathbf{v} \cdot \mathbf{r} c \; d^2 r|_{t=0} + \mathcal{O}(t^3), \end{aligned}$$

where we first take the derivative and then evaluate at the initial time. We realize that the linear term cancels because the flow is incompressible, and the initial concentration field is radially symmetric. To compute the second term, we must calculate the time derivative, and so, changing to polar coordinates, we will have the following:

$$\begin{aligned} \partial_t \int_A \mathbf{v} \cdot \mathbf{r} c \; d^2 r &= 0 + \int v_r r^2 \partial_t c \; dr d\theta \\ &= \int_A v_r r^2 (D \nabla^2 c - \mathbf{v} \cdot \nabla c) dr d\theta, \end{aligned}$$

where the integral of the time derivative of the velocity flow cancels for the same reason as before: flow incompressibility, provided that the symmetry of the initial condition of the concentration is radial. We have used the advection-diffusion equation to get to the last expression. We realize that, again, provided the right symmetry of the initial condition, the term with the diffusion constant is zero. Then, we are only left with the term:

$$\int_A r^2 v_r^2 \partial_r c \; dr d\theta = -\frac{1}{\sigma^2} \int_A (\mathbf{v} \cdot \mathbf{r})^2 c \; d^2 r|_{t=0},$$

where σ^2 was the variance of the concentration field, initially with a Gaussian shape.

Therefore, putting all things together, we get the expression (10) that shows a purely diffusive transient followed by a ballistic transient only dependent on the advective flow:

$$\overline{r^2} = 4Dt + \frac{t^2}{\sigma^2} \int_A (\mathbf{v} \cdot \mathbf{r})^2 c \; d^2 r|_{t=0} + \mathcal{O}(t^3).$$

C. Particles approach of the MSD

To arrive at the relationship given in (11) of the mean squared displacement with the autocorrelation function $g(\tau)$ computed with

$$g(\tau) = \frac{1}{\langle |\mathbf{v}|^2 \rangle} \langle \mathbf{v}(\mathbf{s}) \cdot \mathbf{v}(\mathbf{s} + \tau) \rangle,$$

we must start from the definition of the mean squared displacement of a single particle:

$$\overline{r_1^2}(t) = (\mathbf{r}(t) - \mathbf{r}(0))^2 = \Delta t \sum_{i,j=0}^{N} \mathbf{v}_i \mathbf{v}_j,$$

we have changed to a discrete description of the trajectories with Δt the time between steps, so that $t = \Delta t N$.

When we average over all the particle trajectories, multiply and divide by the average velocity, and rewrite the summation with the diagonal terms of the symmetric matrix out, we end up with the expression (11):

$$\overline{r^2}(t) = \langle |\mathbf{v}|^2 \rangle \Delta t^2 \big(N + 2 \sum_{i<j}^{N} g(i,j)\big),$$

where $g(i,j)$ is only dependent on the difference: $g(j-i)$, when we are at the stationary state.

ACKNOWLEDGMENTS

This project was supported by a collaboration grant with UBICS. I would like to express my deepest gratitude to Jaume and Giacomo for their invaluable guidance and enthusiasm, both in developing this work and in providing career advice. Special thanks also go to my family and friends for their constant support and encouragement.

[1] U. Frisch. *Turbulence: The Legacy of A. N. Kolmogorov*. Cambridge University Press, Cambridge, UK, 1995.

[2] H. Rose and P. Sulem. Nonlinear evolution of instabilities in plasma and fluids. *Journal de Physique*, 39:441–484, 1978.

[3] G. Falkovich and K. R. Sreenivasan. Lessons from hydrodynamic turbulence. *Physics Today*, 59(4):43–49, 2006.

[4] C. Dombrowski, L. Cisneros, S. Chatkaew, R. E. Goldstein, and J. O. Kessler. Self-concentration and large-scale coherence in bacterial dynamics. *Physical Review Letters*, 93(9):098103, 2004.

[5] Ricard Alert, Jaume Casademunt, and Jean-François Joanny. Active turbulence. *Annual Review of Condensed Matter Physics*, 13(Volume 13, 2022):143–170, 2022.

[6] Ido Lavi, Ricard Alert, Jean-François Joanny, and Jaume Casademunt. Dynamical arrest in active nematic turbulence, 2024.

[7] Luca Giomi. Geometry and topology of turbulence in active nematics. *Phys. Rev. X*, 5:031003, Jul 2015.

[8] Ricard Alert, Jean-François Joanny, and Jaume Casademunt. Universal scaling of active nematic turbulence. *Nature Physics*, 16(6):682–688, 2020.

[9] Christopher Dombrowski, Luis Cisneros, Sunita Chatkaew, Raymond E. Goldstein, and John O. Kessler. Self-concentration and large-scale coherence in bacterial dynamics. *Phys. Rev. Lett.*, 93:098103, Aug 2004.

[10] Adama Creppy, Olivier Praud, Xavier Druart, Philippa L. Kohnke, and Franck Plouraboué. Turbulence of swarming sperm. *Phys. Rev. E*, 92:032722, Sep 2015.

[11] Tim Sanchez, Daniel T. N. Chen, Stephen J. DeCamp, Michael Heymann, and Zvonimir Dogic. Spontaneous motion in hierarchically assembled active matter. *Nature*, 491(7424):431–434, November 2012. Epub 2012 Nov 7.

[12] Amin Doostmohammadi and Julia Yeomans. Coherent motion of dense active matter. *The European Physical Journal Special Topics*, 227:2401–2411, 03 2019.

[13] Daiki Nishiguchi and Masaki Sano. Mesoscopic turbulence and local order in janus particles self-propelling under an ac electric field. *Phys. Rev. E*, 92:052309, Nov 2015.

[14] Ido Lavi, Ricard Alert, Jean-François Joanny, and Jaume Casademunt. Nonlinear spontaneous flow instability in active nematics. *arXiv preprint arXiv:2403.16841*, 2024.

[15] Emmanuel Villermaux. Mixing versus stirring. *Annual Review of Fluid Mechanics*, 51(Volume 51, 2019):245–273, 2019.

[16] Y. B. Zel'dovich. The asymptotic law of heat transfer at small velocities in the finite domain problem. *Zhurnal Eksperimental'noi i Teoreticheskoi Fiziki*, 7:1466–1468, 1937.

[17] Rahul Chajwa, Rajarshi, Sriram Ramaswamy, and Rama Govindarajan. Active caustics. *arXiv preprint arXiv:2310.01829*, 2023.

[18] Andrea Villa-Torrealba, Cristóbal Chávez-Raby, Pablo de Castro, and Rodrigo Soto. Run-and-tumble bacteria slowly approaching the diffusive regime. *Phys. Rev. E*, 101:062607, Jun 2020.